Volume 3
Number 2
February 2024
Pages 147–348

Environmental Science Advances

rsc.li/esadvances

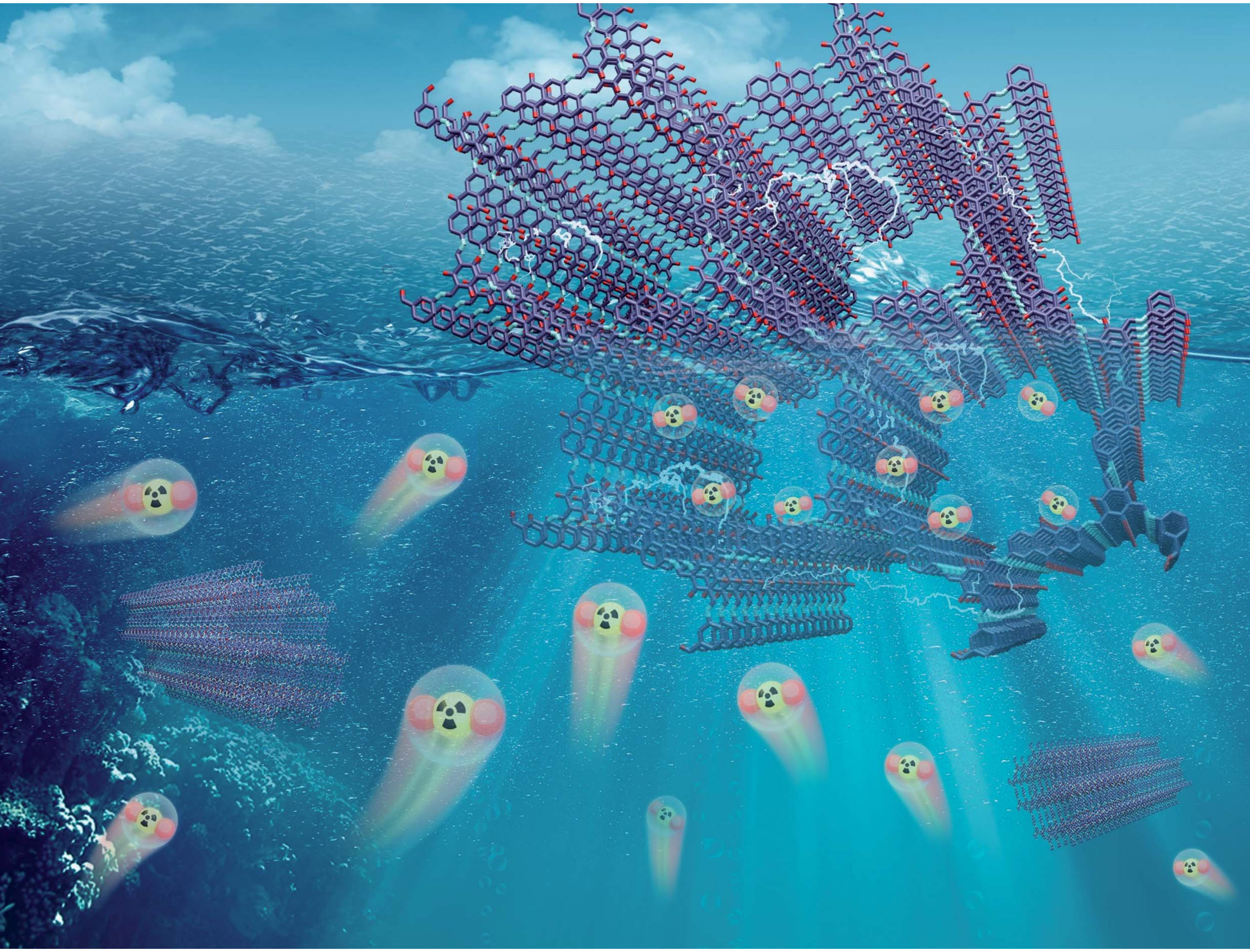

ISSN 2754-7000

ROYAL SOCIETY OF **CHEMISTRY**

PAPER
Yuejie Ai, Xiangke Wang *et al.*
Identification of oxygen sites in β-ketoenamine-linked covalent organic frameworks for highly efficient uranium adsorption through experimental and theoretical studies

Environmental Science
Advances

PAPER

View Article Online
View Journal | View Issue

Check for updates

Cite this: *Environ. Sci.: Adv.*, 2024, **3**, 177

Received 21st October 2023
Accepted 28th November 2023

DOI: 10.1039/d3va00324h

rsc.li/esadvances

Identification of oxygen sites in β-ketoenamine-linked covalent organic frameworks for highly efficient uranium adsorption through experimental and theoretical studies†

Tao Wen, ‡ Xinjie Ma,‡ Yingzhong Huo, Ruoxuan Guo, Sai Zhang, Yanan Han, Yang Liu, Yuejie Ai * and Xiangke Wang *

Anthropogenic activities involving unintended uranium leakage from nuclear accidents, large-scale uranium mining, or nuclear weapon production have caused health and environmental concerns. The increasing demand for highly efficient materials to dispose of uranium may facilitate the sustainable development of nuclear power plants. Herein, a β-ketoenamine-linked covalent organic framework (COF) material, named DQTP COF, was solvothermally synthesized by an imine condensation of 1,3,5-triformylphloroglucinol (TFP) and 2,6-diaminoanthraquinone (DAAQ). The chemical and physical properties of the synthesized DQTP COF were analyzed using various advanced techniques. Additionally, the adsorption behaviors of DQTP COF for U(VI) were optimized by varying parameters, such as pH, ionic strength, contaminant concentration, and reaction temperature. The produced DQTP COF showed an enhanced adsorption capacity of 517.62 mg g^{-1} at pH 6.0 towards U(VI), outperforming most of the currently reported COF-based materials. Moreover, DQTP COF exhibited favorable thermodynamics and excellent anti-ion interference properties as well as good reusability. Experimental analysis and theoretical DFT calculations revealed that UO_2^{2+} ions were bound exclusively by carbonyl groups *via* intramolecular coordination and electrostatic interaction in DQTP COF. This work paves the way to rationally develop functionalized COFs and highlights the potential of COFs for environmental remediation.

Environmental significance

Uranium extraction from water can potentially reduce the negative environmental impact in response to the growing demand for nuclear fuel and the complexity of nuclear waste management. Covalent organic framework (COF) materials are emerging as potential adsorbents in radionuclide immobilization owing to their chemical stability and diversity of organic building units. This work evaluates the adsorption performance of β-ketoenamine-linked COF towards U(VI). The maximum adsorption capacity of 517.62 mg g^{-1} was achieved on the synthesized DQTP COF. More detail, UO_2^{2+} was bounded by carbonyl group in DQTP *via* intramolecular coordination. These findings can extend new perspective for the preparation of other functional COF-based materials for radionuclides cleanup.

1 Introduction

The search for alternatives to fossil fuels has become urgent in the face of fossil energy shortages and global warming. Nuclear power, as a kind of highly efficient clean energy, has become one of the main subjects of concern.[1–3] However, the environmental pollution associated with the development of nuclear energy, such as groundwater pollution from nuclear fuel reprocessing and radionuclide waste leakage from nuclear power plant accidents, cannot be ignored.[4–7] As the primary source of the nuclear industry, the soluble and mobile uranium has been a serious threat to ecological balance and human health.[6,7] Therefore, it is necessary to efficiently reduce and recover uranium from wastewater.

Over the past decades, numerous approaches have been applied in the treatment of uranium, such as catalysis, electrolysis, membrane separation, ion exchange, and adsorption.[8–13] Owing to its advantages of low cost, simple operation, and environmental friendliness, adsorption technology has received widespread attention.[14–16] Traditional adsorption materials, such as zeolites,[17] clays,[18] activated carbons,[19] and metal oxides,[20] have the limitations of low crystallinity, limited surface area, sluggish kinetics, and poor adsorption capacity.

MOE Key Laboratory of Resources and Environmental Systems Optimization, College of Environment and Chemical Engineering, North China Electric Power University, Beijing 102206, P. R. China. E-mail: aiyuejie314@126.com; xkwang@ncepu.edu.cn

† Electronic supplementary information (ESI) available. See DOI: https://doi.org/10.1039/d3va00324h

‡ T. Wen and X. J. Ma contributed equally to this work.

Emerging covalent organic frameworks (COFs) are assembled by organic porous crystalline polymers forming strong covalent bonds with light elements (H, C, O, N, *etc.*). It possesses high crystallization, large specific surface area, well-defined porosity, and outstanding tunable scaffolds.[21–25] Tunable molecular design of various organic linkers enables the COFs as a novel platform among the myriad of research fields, such as energy storage,[26] sensors,[27] membrane separation,[28] adsorption,[29,30] and other applications. Among them, 2,6-diaminoanthraquinone-1,3,5-triformylphloroglucinol, denoted as DQTP COF, is a type of COF material linked by β-ketoenamines through the Schiff base reaction of 1,3,5-triformylphloroglucinol (TFP) and 2,6-diaminoanthraquinone (DAAQ). For DQTP COF, the general advantages of COFs, such as high crystallinity, outstanding porosity, and good thermal stability are well preserved. More importantly, the quinone group in DQTP COF can alter the electronic structure and chemical characteristics of the COF material, exhibiting redox capability and electro-activity. For instance, Chang *et al.* reported that DQTP COF served as a highly efficient electrocatalyst for boosting its oxygen evolution reaction (OER).[31] Huang *et al.* developed DQTP/pencil graphite electrode composite with high catalytic activity for detecting bisphenol A and bisphenol S in the environment.[32] Simultaneously, the two-dimensional periodic π-arrays of DQTP-COF improve the conductivity of π channel in the COF, which have been utilized in the study of electrochemical sensing of hydrazine.

In light of the above applications, DQTP COF as an effective adsorbent has been applied in mitigating environmental problems. Liang *et al.* applied DQTP COF to remove soluble hydrazine, and its maximum adsorption capacity could reach up to 1108 mg g^{-1}.[33] Other studies indicated that the hydrogen bonding and π–π interaction were expected to be key mechanisms behind the high removal efficiency of bisphenol A and hormone.[34,35] In addition to experimental results, Khedri *et al.* combined molecular dynamics simulations, coarse-grained simulations, and density functional theory calculations (DFT) to reveal the adsorption capability of DQTP COF/MOF composite on phenazopyridine (PHP) molecules.[36] The zero charge point (pH_{zpc}) of DQTP COF was found to be 2.3, indicating that there are abundant negative charges on the surface of DQTP COF in both acidic and alkaline environments. On account of the substantial merits of COFs and the quinone group, such COFs may hold an excellent combination of properties that can be employed as the expedient candidate for removing uranyl ions.

By realizing these, we pave the way to systematically investigate the adsorption behavior of uranyl ions on DQTP COF through batch experiments and DFT calculations. In this study, the outstanding DQTP COF was synthesized with excellent physicochemical properties and thermal stability. Furthermore, we investigated the adsorption performance and interaction mechanism of DQTP COF for U(VI). The adsorption process and kinetics of DQTP COF were systematically investigated by batch experiments. The saturation adsorption capacity of DQTP COF reached 517.62 mg g^{-1} at room temperature, and DQTP COF showed good anti-cation interference ability and reusability after 6 adsorption–desorption cycles. Combining batch experiments and static DFT calculations, the main adsorption mechanism was the electrostatic interactions between the carbonyl groups in β-ketoenamine or quinone units and U(VI). This work provides a candidate adsorbent for U(VI) removal from wastewater, proposing experimental and theoretical supports for the potential of covalent organic frameworks in environmental remediation.

2 Materials and methods

2.1 Reagents and instruments

Tetrahydrofuran, mesitylene, dimethylacetamide, ethanol, acetic acid (AcOH), HNO_3, HCl, and NaOH were purchased from Aladdin (Shanghai, China), 1,3,5-triformylphloroglucinol (TFP) was purchased from Yanshen (Jilin, China). 2,6-Diaminoanthraquinone (DAAQ) was purchased from Macklin (Shanghai, China). All reagents were directly used without further purification.

The X-ray diffraction pattern (XRD) was obtained on a Rigaku SmartLab SE (Cu Kα radiation, $\lambda = 1.54$ Å) instrument at a scanning speed of 5° min^{-1}. The 2θ value was set from 2° to 50°. The Fourier transform infrared (FT-IR) spectra were obtained using the IR Tracer 100 spectrometer. Scanning electron microscopy (SEM) was performed on a TESCAN MIRA LMS instrument. The porosity and Brunauer–Emmett–Teller (BET) surface area were measured on TriStar II using the N_2 adsorption–desorption method. Thermogravimetric analysis (TGA) was performed on the STA 2500 analyzer. X-ray photoelectron spectroscopy (XPS) was performed on a Thermo ESCALAB 250XI (Al Kα radiation). Zeta potential analysis was performed on a Zetasizer Nano ZSE instrument.

2.2 Synthesis of DQTP COF

In a typical co-condensation of TFP and DAAQ, TFP (0.3 mmol) and DAAQ (0.4 mmol) were added into a thick-walled pressure bottle with dimethylacetamide (3 mL), mesitylene (1 mL), and AcOH (0.5 mL, 6 M). The obtained suspension was ultrasonically treated for 10 minutes. Afterward, the bottle was degassed by freeze–pump–thaw cycles several times, sealed under a vacuum, and finally heated at 393 K for 3 d. After cooling to room temperature, the mixture containing DQTP COF was washed with dimethylacetamide, tetrahydrofuran, and ethanol three times. The dark red product of DQTP COF was dried at 333 K under vacuum for 12 h.

2.3 Batch adsorption experiments

Batch experiments were conducted to explore the adsorption of uranyl ions on DQTP COF. The effect of the solution pH was investigated using HNO_3/NaOH (0.01–1 M) to adjust the pH value (2.0–11.0). The subsequent batch experiments were performed at the optimal pH value (pH = 6.0). The ionic strength was controlled by adjusting the $NaNO_3$ concentration between 0.001–0.1 M at 298 K. To study the thermodynamic properties of the adsorbent, the initial concentrations of U(VI) were set from 10 ppm to 300 ppm, and the temperature was set at 298, 308, and 318 K. To explore the impact of the co-existing ions on the adsorption for U(VI), a series of aqueous solutions containing 100 mg L^{-1} of one type of ions (Na^+, K^+, Cs^+, Cu^{2+}, Co^{2+}, and Mg^{2+}) and 10 mg L^{-1} of U(VI) were prepared. The above adsorption experiments were performed in a thermostatic shaker for 24 h, with a rotation speed of 200 rpm. For the kinetic analysis, the adsorption time was changed in the range of 0–180 min. After the completion of each adsorption experiment, the supernatant was obtained by membrane filtration, and the concentration of U(VI) was determined using the arsenazo(III) spectrophotometric method. For the reusability analysis, the material was fully eluted with 0.1 M HNO_3 solution and then washed with ultrapure water to neutralize. The removal rate and equilibrium adsorption capacity (q_e) were determined using eqn (1) and (2), respectively.

$$\text{Removal }(\%) = \frac{(C_0 - C_e)}{C_0} \times 100\% \tag{1}$$

$$q_e(\text{mg g}^{-1}) = \frac{V \times (C_0 - C_e)}{w} \tag{2}$$

where C_0 and C_e (mg L^{-1}) represent the initial concentration and equilibrium concentration of U(VI), respectively, V (L) is the solution volume, and w (g) is the adsorbent weight. In addition, all batch experiments were repeated at least three times.

2.4 Computational details

The optimal adsorption configurations and corresponding adsorption energies were derived by the density functional theory (DFT) method with the Vienna *ab initio* Simulation Package (VASP).[37] The Perdew–Burke–Ernzerhof (PBE) functional within the generalized gradient approximation (GGA) was fulfilled to characterize the exchange-correlation potential with a cut-off energy of 400 eV.[38,39] NO_3^- in the experiment was selected to ensure that the whole system was electrically neutral. The 3 × 3 × 1 Monkhorst–Pack (MP) grid was employed for the sampling of the Brillouin zone (BZ). The lattice parameters of DQTP COF were set as $a = b = 29.83$ Å, $c = 3.31$ Å, $\alpha = \beta = 90°$, $\gamma = 120°$, according to the experimental XRD data. In the case of Z-direction, a vacuum region of 15 Å was set to prevent the interactions of those adjacent atoms in the periodic structures. 10^{-5} eV and 0.02 eV $Å^{-1}$ served as the iterative convergence criterion of the energy and forces, respectively. The electrostatic potential (ESP) was explored using the Multiwfn software and visualized by the Visual Molecular Dynamics (VMD) software.[40,41] The adsorption energy (E_{ads}) was calculated using eqn (3):

$$E_{ads} = E_{DQTP@U(VI)} - (E_{DQTP} + E_{U(VI)}) \tag{3}$$

where $E_{DQTP@U(VI)}$ is the total energy of the DQTP COF and U(VI) complex. E_{DQTP} and $E_{U(VI)}$ are the energies of independent DQTP COF and U(VI), respectively.

3 Results and discussion

3.1 Characterizations of DQTP COF

The 2D DQTP COF was solvothermally synthesized by an imine condensation of TFP and DAAQ in a dimethylacetamide/mesitylene/AcOH solvent mixture at 393 K for three days, as shown in the schematic illustration of Fig. 1(a). SEM images were recorded to investigate the morphology and microstructure of DQTP COF (Fig. 1(b) and (c)). It is clear that DQTP COF was composed of cross-linked uniform nanofibers with a diameter of about 23.05 nm, shaped like coral clusters, and the various porosity structures were also clearly visible in the SEM images.

The crystalline nature of DQTP COF was characterized by XRD combing theoretical calculations. The strong diffraction peaks at 3.70°, 6.02°, 7.33°, and 26.92°, shown in Fig. 2(a), correspond to the (100), (110), (200), and (001) crystal facets, respectively. Based on the Bragg equation, the π–π stacking distance was found to be 3.31 Å. The theoretical XRD data based on the AA and AB stacking models were compared in Fig. 2(a), which were obtained from Materials Studio. The experimental XRD pattern matched well with the simulated AA stacking model, which was further verified by the Pawley refinement (R_p = 1.81%, R_{wp} = 2.32%). Therefore, the as-prepared DQTP COF material presented a well-AA stacking framework.

FT-IR was employed to ascertain the chemical composition and structural details of DQTP COF. From Fig. 2(b), the signals at 3332 and 3427 cm^{-1} were assigned to the stretching vibrations of the N–H bond of the DAAQ monomer, and the vibration identified at 1600–1700 cm^{-1} was attributed to the stretching vibration of the C=O bond of the TFP monomer. In the FT-IR spectrum of DQTP COF, the C=C and C–N characteristic peaks at 1554 and 1250 cm^{-1} appeared respectively, while the N–H stretching vibration peak vanished, implying the formation of a stable keto form of Schiff base.[22]

The pore size distribution and specific surface area of DQTP COF were investigated from N_2 adsorption–desorption isotherm measurements at 77 K. As shown in Fig. 2(c), the plotted curves were in accordance with type-IV isotherm, and the adsorption–desorption process exhibited traits of a type H4 hysteresis loop, which are expected to provide mesoporous properties to the adsorbent materials. Based on the nonlocal density functional theory (NLDFT), the Brunauer–Emmett–Teller (BET) surface area of DQTP COF was up to 619 m^2 g^{-1}, and the pore size distributions were centered at 1.73 and 2.06 nm with an average pore size of approximately 1.90 nm, which agreed with the previous experiments.[32] The large specific surface area and uniform distribution of the pore channel in DQTP COF provide the possibility to promote the migration of uranyl ions, which will improve the adsorption rate and capacity of the adsorbent.

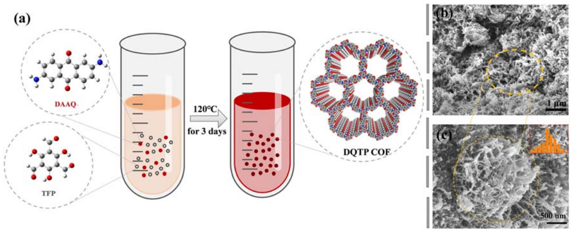

Fig. 1 (a) Schematic diagram of DQTP COF. Low-magnification (b) and high-magnification (c) SEM images of DQTP COF.

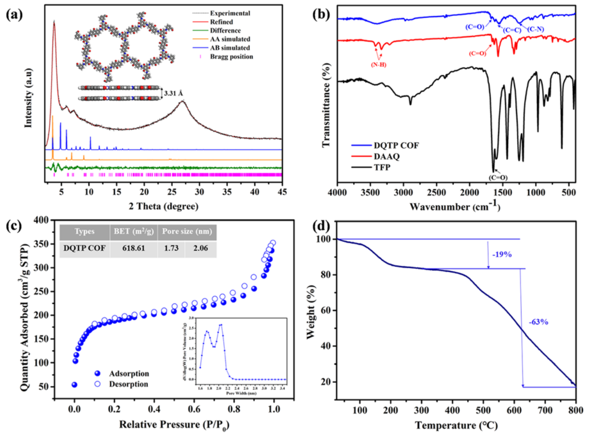

Fig. 2 (a) Overlay of the experimental and calculated XRD traces obtained for DQTP COF, (b) FT-IR spectra of TFP, DAAQ, and DQTP COF, (c) N_2 adsorption–desorption isotherms and the pore size distribution of DQTP COF, (d) the TGA curve of DQTP COF.

TGA revealed the thermal stability of the material (Fig. 2(d)). DQTP COF maintained good thermal stability up to 450 °C. There were two distinct stages of weight loss in DQTP COF: the first stage occurred between 100 °C and 200 °C, with the mass loss of the DQTP COF being around 19%, which was likely caused by the adsorption of moisture from the environment and the evaporation of the residual solvent. A significant weight loss occurred above 450 °C, which was likely caused by the collapse and fracture of the carbon skeleton. In addition to thermal stability, we also assessed the chemical stability of DQTP COF. As shown in Fig. S1,† the two characteristic peaks at 3.70° and 26.92° were maintained in the XRD pattern after immersing DQTP COF in 3 M NaOH and 6 M HCl for three days, indicating that the crystal structure of DQTP COF was not changed in the acidic and alkaline environments. This paves the way for the use of DQTP COF in extreme environments.

3.2 Adsorption performance

3.2.1 Effect of contact time. U(VI) ions were quickly adsorbed on DQTP COF within the first contact of 10 min, and the adsorption equilibrium was reached after 1 h with the adsorption efficiency of over 95% (Fig. 3(a)). The adsorption process of U(VI) on DQTP COF could be divided into two distinct stages: a steep removal stage followed by a steady increase stage until the state of equilibrium was reached. The first stage was predominantly dependent on the diffusion of U(VI) and the electrostatic attraction. Owing to the electrostatic attraction, the dissociated U(VI) ions were immediately adsorbed by DQTP COF in the initial 20 minutes stage of adsorption. The rate of U(VI) adsorption was gradually decreased after 20 min as the adsorption sites on the surface layer became exhausted, and the diffusion of U(VI) from the surface of DQTP COF into the pores resulted in the steady increase stage until it reached the adsorption equilibrium. Typical pseudo-first-order and pseudo-second-order models were used to fit these data to evaluate the kinetic behavior of the adsorption process, eqn (4) and (5) were used to describe both models, respectively.

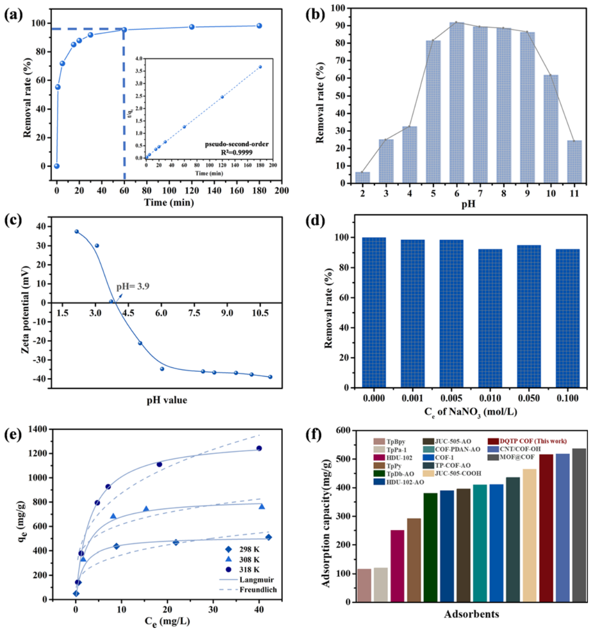

Fig. 3 (a) Adsorption kinetics of U(VI) on DQTP COF. The insets show the corresponding fitting of adsorption kinetics by the pseudo-second-order kinetic model. Conditions: $C_{U(VI)} = 10$ ppm, $m/V = 0.2$ g L^{-1}, pH = 6.0 ± 0.1, $T = 298$ K. (b) Effect of pH on the U(VI) adsorption for DQTP COF. (c) Zeta potential of DQTP COF. (d) Effect of ionic strengths on the U(VI) adsorption for the DQTP COF, (e) adsorption isotherms of U(VI) on DQTP COF by Langmuir (solid lines) and Freundlich (dashed lines) models. (f) Comparison of adsorption capacities with other COF-based materials.

$$\ln(q_e - q_t) = \ln q_e - k_1 t \tag{4}$$

$$\frac{t}{q_t} = \frac{1}{k_2 {q_e}^2} + \frac{t}{q_e} \tag{5}$$

where k_1 (min^{-1}) and k_2 (g (mg^{-1} min^{-1})) are the adsorption rate constants in the pseudo-first-order and pseudo-second-order models, respectively. q_t (mg g^{-1}) and q_e (mg g^{-1}) are the adsorption capacities at time t and adsorption equilibrium, respectively. The parameters are listed in Table 1. From Fig. 3(a) and S2,† the kinetics of U(VI) adsorption on DQTP COF can be predicted using a pseudo-second-order kinetic based on a high correlation coefficient (R^2 = 0.999), which suggested that chemisorption predominates the adsorption between U(VI) and DQTP COF and that the adsorption process was dominated by the strong surface complexation and/or electrostatic interaction.[42]

3.2.2 Effect of pH and ionic strengths. The pH value has a significant impact on the adsorption process since it may affect the surface chemistry of both U(VI) and DQTP COF. The variation of the adsorption performance of U(VI) on DQTP COF in the range of pH = 2.0 to 11.0 was experimentally investigated. The removal rate of U(VI) over DQTP COF increased with the increasing pH from 2.0 to 6.0, followed by a subsequent decline from 6.0 to 11.0 (Fig. 3(b)). The maximum removal rate of about

Table 1 Parameters of the kinetic models for U(VI) adsorption on DQTP COF

Pseudo-first-order			Pseudo-second-order		
k_1 (min^{-1})	q_e (mg g^{-1})	R^2	k_2 (g mg^{-1} mg^{-1})	q_e (mg g^{-1})	R^2
0.04401	15.49	0.9105	9.827×10^{-4}	49.55	0.9999

92% was achieved at pH = 6.0. The adsorption mechanism was related to the distribution of U(VI) species and the surface charge properties of DQTP COF in aqueous solutions. The distribution of the hydrolysis products of U(VI) species is shown in Fig. S3,† positively charged U(VI) species, such as UO_2^{2+}, $UO_2(OH)^+$ and $(UO_2)_3(OH)_5^+$, existed at pH ≤ 6.0. According to Fig. 3(c), the zeta potentials of DQTP COF changed from +40 mV to −40 mV in the pH range of 2.0–11.0. The pH_{zpc} value of DQTP COF was calculated to be 3.9. As a result, the interaction between DQTP COF and U(VI) species gradually transformed from the electrostatic repulsion (pH ≤ 4.0) to the electrostatic attraction (4.0 < pH ≤ 6.0), leading to increased adsorption capacity of DQTP COF for U(VI) in the pH of 2.0 to 6.0. On the other hand, the environment in pH = 6.0 marked the turning point. As the pH increased from 6.0 to 11.0, the predominant U(VI) species were negatively charged, such as $UO_2(OH)_4^{2-}$, $(UO_2)_3(OH)_7^-$ and $UO_2(OH)_3^-$, which was not beneficial for the adsorption process, due to the enhanced electrostatic repulsion between the negative surface charge of DQTP COF and U(VI) species. As shown in Fig. 3(d), the ionic strength showed no obvious impact of U(VI) adsorption onto DQTP COF, indicating that the adsorption process was governed by inner sphere complexation, which was predominantly dependent on pH values and was independent of ionic strengths.

3.2.3 Adsorption isotherm. Adsorption isotherms are also essential to investigate the interaction mechanism between U(VI) and DQTP COF. The adsorption capacity of DQTP COF for U(VI) ions gradually elevated with the increase in temperature from 298 K to 318 K (Fig. 3(e)), suggesting that the adsorption reaction was an endothermic process. The results showed that the adsorption capacity of U(VI) ions by DQTP COF exhibited positive concentration-dependent trends, which could be ascribed to the formation of a concentration gradient between the U(VI) ions and the surface of DQTP COF. However, as the adsorption sites became saturated, the increase in the adsorption capacity gradually decelerated and eventually a dynamic balance was achieved, as a result of the maximum adsorption capacity of 517.62 mg g^{-1} at T = 298 K. The isothermal adsorption model of Langmuir (eqn (6)) and Freundlich (eqn (7)) models were used to simulate the adsorption process of DQTP COF:

$$\text{Langmuir model}: \frac{1}{q_e} = \frac{1}{q_{\max}} + \frac{1}{q_{\max}k_L} \times \frac{1}{C_e} \qquad (6)$$

$$\text{Freundlich model}: \ln q_e = \ln k_F + \frac{1}{n}\ln C_e \qquad (7)$$

where k_L (L mg^{-1}) is the Langmuir equilibrium constants, k_F (L mg^{-1}) and n are the Freundlich parameters. q_e and $q_{\max}$ are the equilibrium and maximum adsorption capacities (mg g^{-1}), respectively. C_e (mg L^{-1}) is the equilibrium concentration. The relative thermodynamic functions (the free energy change ~ΔG^0, the enthalpy change ~ΔS^0, and the enthalpy change ~ΔH^0) were calculated from the correlation equations (as listed in ESI†). According to the linear plots of ln K^0 *vs.* 1/T (Fig. S4†), the fitting thermodynamic functions were correspondingly calculated. The positive values of ΔH^0 (55.15 kJ mol^{-1}) and ~ΔS^0 (277.43 J mol^{-1} K^{-1}) demonstrated that the adsorption of U(VI) on DQTP COF was an endothermic and spontaneous process. The mean negative ΔG^0 decreased from −27.52 kJ mol^{-1} to −33.07 kJ mol^{-1} with increasing temperature, suggesting that the spontaneous nature of the interaction is inversely proportional to the temperature.

From the results in Fig. 3 and Table 2, the Langmuir model is more consistent with experimental data. This phenomenon demonstrated that the adsorbent-bound uranium is a homogeneous monolayer interaction process, which mainly occurs on the functional groups and active sites of DQTP COF.[43] Compared to most reported COF materials (shown in Fig. 3(f) and Table S1†), DQTP COF had a better adsorption capacity for U(VI), which is a candidate adsorbent for wastewater remediation.

3.2.4 Effect of co-existing ions and recycling of DQTP COF. In real wastewater conditions, there are several extra metal ions in addition to U(VI), including Na$^+$, K$^+$, Cs$^+$, Cu^{2+}, Co^{2+}, and Mg^{2+}. The competitive adsorption of these co-existing ions on the surface of DQTP COF cannot be disregarded. As shown in Fig. 4(a), the DQTP COF had selective adsorption of U(VI) among the numerous competing cations. The image illustrates how the competition impact of the monovalent metal ions such as Na$^+$, K$^+$, Cs$^+$, and U(VI) can be completely disregarded, with DQTP COF showing a high removal efficiency of U(VI) (almost 100%). Probably, the coordination properties and charge density of the monovalent metal cations were significantly different from those of U(VI).[44] However, the bivalent metal ions had a greater significant impact on the extraction of U(VI) by DQTP COF. Furthermore, there was a more obvious competition between

Table 2 Adsorption isotherm parameters for the Langmuir and Freundlich models of U(VI) on DQTP COF

	Langmuir			Freundlich		
T (K)	K_L (L g^{-1})	q_m (mg g^{-1})	R^2	K_F (mg^{1-n} L^n g^{-1})	1/n	R^2
298	0.56	517.62	0.994	190.02	0.286	0.912
308	0.36	831.44	0.971	380.17	0.210	0.684
318	0.32	1326.12	0.998	424.63	0.313	0.883

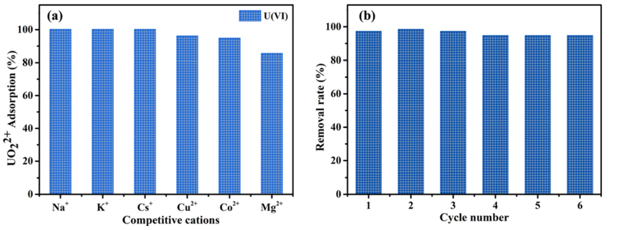

Fig. 4 (a) Effect of co-existing ions for the U(VI) extraction efficiency using DQTP COF. (b) Adsorption cycles of U(VI) onto DQTP COF. Conditions: $C_{U(VI)} = 10$ ppm, $C_{\text{co-existing ions}} = 100$ ppm, $m/V = 0.2$ g L^{-1}, pH = 6.0 ± 0.1, $T = 298$ K.

Mg^{2+} and U(VI) among these co-existing ions. Overall, the DQTP COF showed strong anti-ion interference properties, indicating its suitability as an available adsorbent for wastewater treatment.

To further evaluate the possibility of DQTP COF for the application, we investigated the potential for regeneration and recyclability of DQTP COF bound U(VI). The reusability of the material shown in Fig. 4(b) indicated that DQTP COF still exhibited satisfactory removal performance of U(VI) after six adsorption–desorption cycles, indicating the potential application of DQTP COF for wastewater remediation.

3.3 Adsorption mechanism

To further gain insight into the interaction mechanism between DQTP COF and U(VI), the SEM investigation of U(VI)-laden DQTP COF was performed. Comparing Fig. 5(a) with Fig. 5(b), no obvious change was found in the fundamental structure of DQTP COF after the adsorption of U(VI), suggesting certain mechanical structure stability of DQTP COF.[45,46] Similarly, Fig. 5(c) shows the FT-IR spectrum of DQTP COF after the adsorption of U(VI). The characteristic peaks of DQTP COF after U(VI) adsorption at other positions were essentially unaltered, demonstrating the stability of the DQTP COF structure. Besides, it can be seen that a distinctive O═U═O peak appeared at 911 cm^{-1}, indicating that the U(VI) target ions were successfully adsorbed on the surface of DQTP COF.[47] The XPS spectrum gives more detailed information for the interaction mechanism between the DQTP COF and U(VI). The fine spectra of N 1s (in Fig. 5(d)) showed two distinctive peaks at 400.28 and 399.81 eV that corresponded to C–N and C═N, respectively, demonstrating the successful condensation reaction of the two ligands, TFP and DAAQ. After adsorption, we found that uranyl ions were successfully adsorbed on DQTP COF, as evidenced by the appearance of the distinctive peak for U 4f in the XPS survey spectrum (in Fig. S5†). Furthermore, as illustrated in Fig. 5(e), the U 4f fine pattern demonstrated that the binding energies at 392.89 and 382.08 eV were assigned to U $4f_{5/2}$ and U $4f_{7/2}$, respectively, and that the appearance of the two subpeaks was probably due to multiple splitting of the unpaired electron spins in the atomic shell layer.[48] Moreover, as shown in Fig. 5(f), the fine spectra of O 1s show the characteristic peak for the O–U bond at 531.55 eV after the adsorption of U(VI).[42] The existence of the O–U bond confirmed that the O atom in the DQTP COF

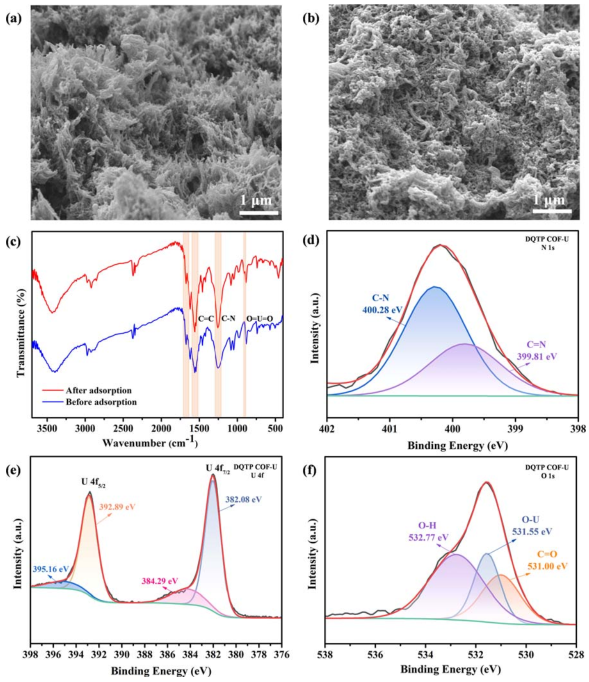

Fig. 5 SEM images of DQTP COF before (a) and after (b) U(VI) adsorption. FT-IR spectra of (c) DQTP COF before and after U(VI) adsorption. (d) N 1s, (e) U 4f, and (f) O 1s XPS spectra of DQTP COF after U(VI) adsorption.

was involved in the complexation between the carbonyl groups and U(VI) ions. Besides, the two typical peaks at 532.77 and 531 eV corresponded to O–H and C═O, respectively.

In order to thoroughly acquire the binding information, DFT calculations were utilized to examine the interaction between uranyl ions and DQTP COF in terms of the adsorption configurations, energies, and electronic characteristics. Firstly, the electrostatic potential (ESP) map was applied to identify the potential adsorption sites for uranyl ions. As shown in Fig. 6(a), two kinds of negative electrostatic potentials are present in the DQTP COF, which are the carbonyl groups in β-ketoenamine and quinone units, and their electrostatic potentials are −29.1 kcal mol^{-1} and −32.67 kcal mol^{-1}, respectively. It can be concluded that these two are crucial regions for the interaction

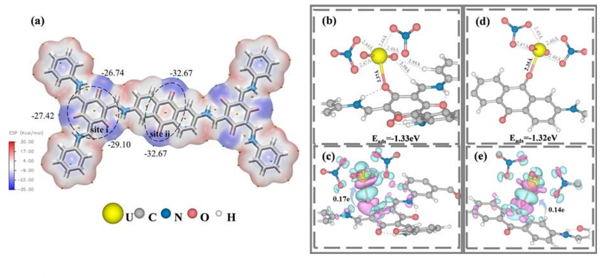

Fig. 6 (a) ESP map of DQTP COF. The positive and negative electrostatic potentials are represented by the red and blue zones, respectively. The optimized geometries (b) and difference charge density (c) of U(VI) adsorbed by the β-ketoenamine unit (site i). The optimized geometries (d) and difference charge density (e) of U(VI) adsorbed by the quinone unit (site ii).

with U(VI), which agrees with the experimental observations discussed above.

Fig. 6(b)–(d) shows the optimized geometries of DQTP COF interacting with U(VI). The U atom mainly interacted with the O atom of carbonyl groups in β-ketoenamine and quinone units. The U–O bond lengths in the β-ketoenamineand quinone units are 2.37 Å and 2.35 Å, and the corresponding adsorption energy values are −1.33 eV and −1.32 eV, respectively. Moreover, a significant charge transfer was observed between the carbonyl groups in β-ketoenamine (quinone units) and uranyl ions, 0.17 e and 0.14 e, respectively, which is in line with the results of the experiment. In addition to the coordination interactions between DQTP COF and U(VI), a hydrogen bond network also existed in the β-ketoenamine unit with bond lengths of around 2.35–2.55 Å, as shown in Fig. 6(b). In conclusion, DFT calculations showed that the main interaction mechanism between DQTP COF and uranyl ion is the synergistic effect of electrostatic and coordination interactions. Hydrogen bonding also plays a significant role in the elimination of U(VI).

Conclusions

In this study, a β-ketoenamine-linked covalent organic framework named DQTP COF was synthesized, which exhibited stable physicochemical properties, thermal stability, and outstanding surface area. In particular, for the extraction of uranyl ions, DQTP COF demonstrated exceptional adsorption capacity ($q_{\max} = 517.62$ mg g^{-1}), which was superior to that of the most reported COF-based materials. The adsorption process displayed quick adsorption kinetics, which reached adsorption equilibrium in about 60 min. Moreover, DQTP COF showed high anti-cation interference ability and reusability after six adsorption–desorption cycles. Combining experimental analysis with static DFT calculations, the interaction mechanisms between DQTP COF and U(VI) were clarified as follows: (1) the coordination interactions between uranyl ions and DQTP COF enhanced the adsorption ability; (2) there was a significant charge transfer between the carbonyl groups in DQTP COF and U(VI) ions. In summary, this study proposes an efficient adsorbent for the removal of U(VI) from wastewater, enhancing the potential of covalent organic frameworks for environmental remediation.

Conflicts of interest

The author declares that he has no conflicts of interest.

Acknowledgements

The authors gratefully acknowledge the financial support from the National Natural Science Foundation of China (22076044 and 22106047), Science Challenge Project (no. TZ2016004), and Beijing Outstanding Young Scientist Program.

References

1 K. Kiegiel, L. Steczek and G. Zakrzewska-Trznadel, Application of calixarenes as macrocyclic ligands for uranium(VI): a review, *J. Chem.*, 2013, **2013**, 1–16, DOI: **10.1155/2013/762819**.

2 H. Wang, H. Guo, N. Zhang, Z. Chen, B. Hu and X. Wang, Enhanced photoreduction of U(VI) on C_3N_4 by Cr(VI) and bisphenol A: ESR, XPS, and EXAFS investigation, *Environ. Sci. Technol.*, 2019, **53**, 6454–6461, DOI: **10.1021/acs.est.8b06913**.

3 J. Wang, Y. Wang, W. Wang, T. Peng, J. Liang, P. Li, D. Pan, Q. Fan and W. Wu, Visible light driven Ti^{3+} self-doped TiO_2 for adsorption-photocatalysis of aqueous U(VI), *Environ. Pollut.*, 2020, **262**, 114373, DOI: **10.1016/j.envpol.2020.114373**.

4 Q. Sun, B. Aguila, L. D. Earl, C. Abney, L. Wojtas, P. Thallapally and S. Ma, Covalent organic frameworks as a decorating platform for utilization and affinity enhancement of chelating sites for radionuclide sequestration, *Adv. Mater.*, 2018, **30**, 1705479, DOI: **10.1002/adma.201705479**.

5 C. Zhao, X. Ma, X. Wei, W. Liu, L. Sun and Y. Ai, Effective strategies toward imine-linked cationic covalent organic frameworks for rapid and selective removal of $^{99}TcO_4^-$ from water: insights from DFT and MD calculations, *Environ. Sci.: Nano*, 2023, **10**, 611–624, DOI: **10.1039/d2en01049f**.

6 D. Sun, C. Lv, Y. Hua, M. Li, X. Zhang, Q. Fang, T. Cai and X. Wu, High efficiency electrochemical separation of uranium(VI) from uranium-containing wastewater by microbial fuel cells with different cathodes, *Bioelectrochemistry*, 2023, **151**, 108393, DOI: **10.1016/j.bioelechem.2023.108393**.

7 N. Kobylinska, L. Puzyrnaya and G. Pshinko, Magnetic nanocomposites based on Zn, Al-LDH intercalated with citric and EDTA groups for the removal of U(VI) from environmental and wastewater: synergistic effect and adsorption mechanism study, *RSC Adv.*, 2022, **12**, 32156–32172, DOI: **10.1039/d2ra05503a**.

8 D. Zhao, Z. Peng, J. Fang, Z. Fang and J. Zhang, Programmable and low-cost biohybrid membrane for efficient heavy metal removal from water, *Sep. Purif. Technol.*, 2023, **306**, 122751, DOI: **10.1016/j.seppur.2022.122751**.

9 C. Zhao, J. Liu, Y. Deng, Y. Tian, G. Zhang, J. Liao, J. Yang, Y. Yang, N. Liu and Q. Sun, Uranium(VI) adsorption from aqueous solutions by microorganism-graphene oxide composites via an immobilization approach, *J. Cleaner Prod.*, 2019, **236**, 117624, DOI: **10.1016/j.jclepro.2019.117624**.

10 Z. Jiang, X. Zhang, S. Guo, Y. Zheng, J. Wang, T. Wen and X. Wang, Recent advances and perspectives of emerging two-dimensional transition metal carbide/nitride-based materials for organic pollutant photocatalysis, *Mater. Chem. Front.*, 2023, **7**, 4658–4682, DOI: **10.1039/D3QM00288H**.

11 W. Cui, C. Zhang, R. Xu, X. Chen, W. Jiang, Y. Li, R. Liang, L. Zhang and J. Qiu, Rational design of covalent organic frameworks as a groundbreaking uranium capture platform through three synergistic mechanisms, *Appl.*

Catal., B, 2021, **294**, 120250, DOI: 10.1016/j.apcatb.2021.120250.

12 M. T. Di, X. J. Sun, L. Hu, L. Gao, J. Liu, X. Yan, X. Wu, X. Jiang and G. He, Hollow COF selective layer based flexible composite membranes constructed by an integrated "casting-precipitation-evaporation" strategy, *Adv. Funct. Mater.*, 2022, **32**, 2111594, DOI: 10.1002/adfm.202111594.

13 X. Liu, M. Xiao, Y. Li, Z. Chen, H. Yang and X. Wang, Advanced Porous Materials and Emerging Technologies for Radionuclides Removal from Fukushima Radioactive Water, *Ecol., Environ. Health*, 2023, **2**, 252–256, DOI: 10.1016/j.eehl.2023.09.001.

14 A. Zhang and Y. Ai, Structure control of covalent organic frameworks (COFs) and their applications in environmental chemistry, *Prog. Chem.*, 2020, **32**, 1564–1581, DOI: 10.7536/PC200202.

15 R. Leng, Y. Sun, R. Feng, G. Zhao, Z. Qu, C. Wang, B. Han, J. Wang, Z. Ji and X. Wang, Design and Fabrication of Hypercrosslinked Covalent Organic Adsorbents for Selective Uranium Extraction, *Environ. Sci. Technol.*, 2023, **57**, 9615–9626, DOI: 10.1021/acs.est.3c02916.

16 X. Liu, M. Xiao, Y. Li, Z. Chen, H. Yang and X. Wang, Advanced Porous Materials and Emerging Technologies for Radionuclides Removal from Fukushima Radioactive Water, *Ecol., Environ. Health*, 2023, **2**, 252–256, DOI: 10.1016/j.eehl.2023.09.001.

17 Q. Zhang, Y. Wang, Z. Wang, Z. Zhang, X. Wang and Z. Yang, Active biochar support nano zero-valent iron for efficient removal of U(VI) from sewage water, *J. Alloys Compd.*, 2021, **852**, 156993, DOI: 10.1016/j.jallcom.2020.156993.

18 H. Huawen, K. Muhammad, Z. Tuoyu, R. Xu, O. Masek and X. Li, A critical review of clay-based composites with enhanced adsorption performance for metal and organic pollutants, *J. Hazard. Mater.*, 2019, **369**, 780–796, DOI: 10.1016/j.jhazmat.2019.02.003.

19 P. Zong, S. Wang, Y. Zhao, H. Wang, H. Pan and C. He, Synthesis and application of magnetic graphene/iron oxides composite for the removal of U(VI) from aqueous solutions, *Chem. Eng. J.*, 2013, **220**, 45–52, DOI: 10.1016/j.cej.2013.01.038.

20 J. Neto, C. Bellato and D. Silva, Iron oxide/carbon nanotubes/chitosan magnetic composite film for chromiumspecies removal, *Chemosphere*, 2019, **218**, 391–401, DOI: 10.1016/j.chemosphere.2018.11.080.

21 A. Cote, A. Benin, N. Ockwig, M. O'Keeffe, A. Matzger and O. Yaghi, Porous, crystalline, covalent organic frameworks, *Science*, 2005, **310**, 1166–1170, DOI: 10.1126/science.1120411.

22 C. Wen, Y. Yao, L. Meng, E. Duan, M. Wang, Z. Chen and X. Wang, Photocatalytic and electrocatalytic extraction of uranium by COFs: A review, *Ind. Eng. Chem. Res.*, 2023, **62**, 18230–18250, DOI: 10.1021/acs.iecr.3c02831.

23 X. Liu, A. Zhan g, R. Ma, B. Wu, T. Wen, Y. Ai, M. Sun, J. Jin, S. Wang and X. Wang, Experimental and theoretical insights into copper phthalocyanine-based covalent organic frameworks for highly efficient radioactive iodine capture, *Chin. Chem. Lett.*, 2022, **33**, 3549–3555, DOI: 10.1016/j.cclet.2022.03.001.

24 Z. Chen, J. Wang, M. Hao, Y. Xie, X. Liu, H. Yang, G. I. N. Waterhouse, X. Wang and S. Ma, Tuning excited electronic structure and charge transport in covalent organic frameworks for enhanced photocatalytic performance, *Nat. Commun.*, 2023, **14**, 1106, DOI: 10.1038/s41467-023-36710-x.

25 H. Gu, X. Liu, S. Wang, Z. Chen, H. Yang, B. Hu, C. Shen and X. Wang, COF-based composites: extraordinary removal performance for heavy metals and radionuclides from aqueous solutions, *Rev. Environ. Contam. Toxicol.*, 2022, **260**, 23, DOI: 10.1007/s44169-022-00018-6.

26 L. Li, F. Lu, R. Xue, B. Ma, Q. Li, N. Wu, H. Liu, W. Yao, H. Guo and W. Yang, Ultrastable triazine-based covalent organic framework with an interlayer hydrogen bonding for supercapacitor applications, *ACS Appl. Mater. Interfaces*, 2019, **11**, 26355–26363, DOI: 10.1021/acsami.9b06867.

27 C. Zhang, W. Cui, W. Jiang, F. Li, Y. Wu, R. Liang and J. Qiu, Simultaneous sensitive detection and rapid adsorption of UO_2^{2+} based on a post-modified sp(2) carbon-conjugated covalent organic framework, *Environ. Sci.: Nano*, 2020, **7**, 842–850, DOI: 10.1039/c9en01225g.

28 L. Zhu, C. Zhang, F. Qin, F. Ma, C. Bi, R. Zhu, L. Liu, J. Bai, H. Dong and T. Satoh, Amidoxime-modified hypercrosslinked porous poly(styrene-co-acrylonitrile) adsorbent with tunable porous structure for extracting uranium efficiently from seawater, *J. Mol. Liq.*, 2022, **368**, 120741, DOI: 10.1016/j.molliq.2022.120741.

29 J. Yang, L. Huang, J. You and Y. Yamauchi, Magnetic covalent organic framework composites for wastewater remediation, *Small*, 2023, **19**, 2301044, DOI: 10.1002/smll.202301044.

30 K. Liu, J. Yang, J. Liu, Q. Shuai and Y. Yamauchi, M Han and L Huang. Robust self-floating covalent organic framework/chitosan aerogels for the efficient removal of sulfamerazine, *Chem. Eng. J.*, 2023, **472**, 144966, DOI: 10.1016/j.cej.2023.144966.

31 J. Chang, G. Xu, H. Li and Q. Fang, Quinone-based covalent organic frameworks for efficient oxygen evolution reaction, *Chem. J. Chin. Univ.*, 2020, **41**, 1609–1614, DOI: 10.7503/cjcu2020112.

32 Y. Huang, Y. Pang, X. Shen, R. Jiang and Y. Wang, Covalent organic framework DQTP modified pencil graphite electrode for simultaneous determination of bisphenol A and bisphenol S, *Talanta*, 2022, **236**, 122859, DOI: 10.1016/j.talanta.2021.122859.

33 C. Liang, H. Lin, Q. Wang, E. Shi, S. Zhou, F. Zhang, F. Qu and G. Zhu, A redox-active covalent organic framework for the efficient detection and removal of hydrazine, *J. Hazard. Mater.*, 2020, **381**, 120983, DOI: 10.1016/j.jhazmat.2019.120983.

34 Y. Pang, Y. Huang, X. Shen and Y. Wang, Electro-enhanced solid-phase microextraction with covalent organic framework modified stainless steel fiber for efficient adsorption of bisphenol A, *Anal. Chim. Acta*, 2021, **1142**, 99–107, DOI: 10.1016/j.aca.2020.10.061.

35 N. Li, D. Wu, X. Li, X. Zhou, G. Fan, G. Li and Y. Wu, Effective enrichment and detection of plant growth regulators in fruits and vegetables using a novel magnetic covalent organic framework material as the adsorbents, *Food Chem.*, 2020, **306**, 125455, DOI: **10.1016/j.foodchem.2019.125455**.

36 M. Khedri, R. Maleki, S. Khiavi, M. Ghasemi, E. Ghasemy, A. Jahromi and A. Razmjou, Removal of phenazopyridine as a pharmacological contaminant using nanoporous metal/covalent-organic frameworks (MOF/COF) adsorbent, *Appl. Mater. Today*, 2021, **25**, 101196, DOI: **10.1016/j.apmt.2021.101196**.

37 G. Kresse and J. Furthmüller, Efficiency of ab initio total energy calculations for metals and semiconductors using a plane-wave basis set, *Comput. Mater. Sci.*, 1996, **6**, 15–50, DOI: **10.1016/0927-0256(96)00008-0**.

38 Y. Wang and J. P. Perdew, Accurate and simple analytic representation of the electron-gas correlation energy, *Phys. Rev. B: Condens. Matter Mater. Phys.*, 1992, **45**, 13244–13249, DOI: **10.1103/PhysRevB.45.13244**.

39 J. Furthmüller and G. Kresse, Efficient iterative schemes for ab initio total-energy calculations using a plane-wave basis set, *Phys. Rev. B: Condens. Matter Mater. Phys.*, 1996, **54**, 11169–11186, DOI: **10.1103/PhysRevB.54.11169**.

40 T. Lu and F. Chen, Multiwfn: a multifunctional wavefunction analyzer, *J. Comput. Chem.*, 2012, **33**, 580–592, DOI: **10.1002/jcc.22885**.

41 W. Humphrey, A. Dalke and K. Schulten, VMD: visual molecular dynamics, *J. Mol. Graphics*, 1996, **14**, 33–38, DOI: **10.1016/0263-7855(96)00018-5**.

42 X. Zhong, W. Liang, Z. Lu and B. Hu, Highly efficient enrichment mechanism of U(VI) and Eu(III) by covalent organic frameworks with intramolecular hydrogen-bonding from solutions, *Appl. Surf. Sci.*, 2020, **504**, 144403, DOI: **10.1016/j.apsusc.2019.144403**.

43 Z. D. Li, H. Q. Zhang, X. H. Xiong and F. Luo, U(VI) adsorption onto covalent organic frameworks-TpPa-1, *J. Solid State Chem.*, 2019, **277**, 484–492, DOI: **10.1016/j.jssc.2019.06.044**.

44 Z. Li, R. Zhu, P. Zhang, M. Yang, R. Zhao, Y. Wang, X. Dai and W. Liu, Functionalized polyarylether-based COFs for rapid and selective extraction of uranium from aqueous solution, *Chem. Eng. J.*, 2022, **434**, 134623, DOI: **10.1016/j.cej.2022.134623**.

45 Y. Guo, Z. Gong, C. Li, B. Gao, P. Li, X. Wang, B. Zhang and X. Li, Efficient removal of uranium (VI) by 3D hierarchical Mg/Fe-LDH supported nanoscale hydroxyapatite: A synthetic experimental and mechanism studies, *Chem. Eng. J.*, 2020, **392**, 123682, DOI: **10.1016/j.cej.2019.123682**.

46 X. Liu, Y. Xie, Y. Li, M. Hao, Z. Chen, H. Yang, G. I. N. Waterhouse, S. Ma and X. Wang, Functional Carbon Capsules Supporting Ruthenium Nanoclusters for Efficient Electrocatalytic $^{99}TcO_4^-/ReO_4^-$ Removal from Acidic and Alkaline Nuclear Wastes, *Adv. Sci.*, 2023, 2303536, DOI: **10.1002/advs.202303536**.

47 R. Guo, Y. Liu, Y. Huo, A. Zhang, J. Hong and Y. Ai, Chelating effect between uranyl and pyridine N containing covalent organic frameworks: a combined experimental and DFT approach, *J. Colloid Interface Sci.*, 2022, **606**, 1617–1626, DOI: **10.1016/j.jcis.2021.08.118**.

48 F. Li, W. Cui, W. Jiang, C. Zhang, R. Liang and J. Qiu, Stable sp carbon-conjugated covalent organic framework for detection and efficient adsorption of uranium from radioactive wastewater, *J. Hazard. Mater.*, 2020, **392**, 122333, DOI: **10.1016/j.jhazmat.2020.122333**.